Chemical Engineering Journal 515 (2025) 163167

Contents lists available at ScienceDirect

Chemical Engineering Journal

journal homepage: www.elsevier.com/locate/cej

Climate-friendly hydrogen and carbon production by methane and biogas pyrolysis: Spatial resolution of reactor performance☆

Ahmet Çelik, Akash Bhimrao Shirsath, Manas Mokashi, Jonas Tatzig, Heinz Müller, Olaf Deutschmann, Patrick Lott *

Institute for Chemical Technology and Polymer Chemistry (ITCP), Karlsruhe Institute of Technology (KIT), Engesserstr. 20, 76131 Karlsruhe, Germany

ARTICLE INFO

Keywords:
Methane pyrolysis
Biogas pyrolysis
Hydrogen
Carbon capture
Gas phase profiles
Reaction network

ABSTRACT

The thermal pyrolysis of methane and of biogas as renewable feedstock was investigated through the axial resolution of concentration profiles inside the pyrolysis reactor using a high-temperature capillary-based spatial profiling (SpaciPro) technique. Herein, the mole fraction of main components (H_2, CH_4, CO, CO_2, and H_2O) as well as minor components (C_2H_6, C_2H_4, C_2H_2, and C_6H_6) was studied. Comparing the experimental results with microkinetic simulations allowed conducting a fundamental analysis of the reaction network. Overall, a good agreement between experiments and simulations was achieved for the main components. However, gas phase kinetics could only partly predict the experimental results regarding minor components, which underlines the important role of deposition reactions and soot formation *via* polyaromatic hydrocarbons. For methane as feed gas, coupling these processes with the gas phase mechanism resulted in a fairly accurate prediction of the experimental results, especially for hot zone temperatures above 1200 °C. In the case of biogas as feedstock, additional gas phase reactions become relevant that necessitate an extension of the gas phase mechanism; direct carbon deposition reactions are considered as well. The numerically predicted profiles agree well with the experimentally determined ones over a wide temperature range of 1200 °C to 1600 °C and point to the formation of different reaction regimes that strongly correlate to the temperature profile in the reactor. Herein, the reverse water–gas shift reaction is dominant between the inlet of the reactor and the entrance of the isothermal hot zone, dry reforming is dominant in the subsequent zone, and the pyrolysis reaction becomes dominant in the isothermal hot zone.

1. Introduction

The production of hydrogen is responsible for more than 3 % of the global carbon dioxide (CO_2) emissions [1–3]. In this context, the thermal decomposition of methane-rich feedstocks *via* pyrolysis represents a promising technology for the generation of hydrogen (H_2) and simultaneous carbon capture without causing direct CO_2 emissions. This process also represents a prospective eco-friendly and cost-effective alternative to steam methane reforming (SMR) and electrolysis of water (H_2O) [4–8]. Using biogas, e.g., from the fermentation of biomass, as renewable feedstock leads to a mixture of H_2 and carbon monoxide (CO) as product gas due to the CO_2 content of the biogas [9]. Hereby, the process may serve as effective CO_2 sink and the product gas stream can be used as entirely renewable syngas [10].

The endothermic decomposition of the CH_4 molecule can be realized catalytically [11–13], by means of metal-based catalysts [14,15], or by a thermo-catalytic processes on carbonaceous substrates [11,16–18]. Each configuration bears distinct advantages and drawbacks. While metal-based catalysts facilitate CH_4 activation at lower temperatures (< 800 °C) [14,15], thermal processes require higher temperatures (> 1000 °C) but yield pure carbon without metallic impurities and allow for prolonged operational durations without catalyst degradation [11,19]. Utilizing carbon as a catalyst combines these advantages, enabling a quasi-autocatalytic process wherein carbon predominantly accrues on the initially provided particles [11,20,21]. Beyond the (catalytic) modalities employed, various reactor configurations have been explored in the literature, diverging largely in energy supply strategies and particle flow control. These encompass plasma torches [22,23], liquid salt or liquid metal-based setups [24,25], microwave-assisted systems [26], moving or packed-bed arrangements [27,28], and flow

☆ This article is part of a special issue entitled: 'ISCRE 28' published in Chemical Engineering Journal.

* Corresponding author.
E-mail address: patrick.lott@kit.edu (P. Lott).

https://doi.org/10.1016/j.cej.2025.163167

Available online 28 April 2025

reactors [11,12].

Flow reactors are also particularly interesting from a fundamental scientific point of view, as their comparatively simple structure allows the residence times in the reactor to be precisely adjusted. Variation of the residence time helps to break down reaction paths and to determine essential intermediates. Along these lines, various reaction mechanisms have been proposed for methane pyrolysis, most of which comprise radical formation, dehydrogenation, and coupling steps [29–34]. These mechanisms are used to perform detailed reactor simulations using microkinetic models to predict product compositions under variable reactor conditions. For instance, Mokashi et al. [12] used reaction mechanisms from Appel et al. [29], Golovitchev [35], Norinaga and Deutschmann [31], as well as Porras et al. [36] to investigate gas phase methane pyrolysis. Herein, simulations were compared with experimental end-of-pipe results and deviations were attributed to heterogeneous reactions forming solid carbon that remained unconsidered in the microkinetic models.

Regarding carbon production, two separate, competing mechanisms are relevant: soot formation and direct deposition reactions. Soot formation occurs via hydrogen abstraction and acetylene addition (HACA mechanism) [29,30,37,38], whereby small hydrocarbon radicals polymerize into benzene and larger polyaromatic hydrocarbons (PAHs). The latter eventually condense into primary soot particles and then undergo surface growth and agglomeration. These soot particles can further react, forming larger aggregates and contributing to soot emissions in industrial processes, which can block pipes as well as small units and therefore need to be filtered from the gas phase. Direct deposition, on the other hand, occurs when carbon forms directly on a catalytic or non-catalytic surface. Herein, methane and hydrocarbon intermediates adsorb onto the surface and decompose into carbon and hydrogen (chemical vapor deposition – CVD) [39–43]. The deposited carbon layers can form as amorphous carbon, graphite-like structures, or filamentous carbon. The type of carbon formed strongly depends on the reaction conditions and the nature of the surface. If a catalyst is used, deposition reactions lead to deactivation of the catalyst; in any case, uncontrolled carbon formation can result in blocking of the reactor.

Considering these carbon formation routes, Mokashi and Shirsath et al. [28,44] proposed a model that couples both, gas phase reactions as well as heterogeneous reactions for deposition and soot formation. Even though the simulations were in a good agreement with end-of-pipe experimental results for main products, there were deviations for minor species, such as C_2H_6, C_2H_4, C_2H_2, C_3H_6, C_6H_6, or PAH, which represent all intermediates towards soot formation. These deviations may be explained by the fact that for the above-mentioned simulations solely experimental end-of-pipe results on the product gas composition were available for model development and validation. Experimentally determined spatially resolved gas phase species concentration profiles, which are used widely to study reaction networks [45–51], would provide important insights to close the gap between simulated data and experimental results and lead to a basis for more accurate reactor models. However, recording spatially resolved data for methane pyrolysis poses considerable technical challenges, on the one hand because the high temperatures impede the use of conventional materials, on the other hand because three phases must be considered effectively: Gas phase, intermediate species with high boiling temperatures such as PAH, and solids formation.

The scope of this work is to shed light on the elementary steps that take place during thermal methane pyrolysis by providing spatially resolved data on product gas compositions for various industrially relevant reactor operation points. Beyond methane also biogas is considered as a feedstock, since in addition to pyrolysis also reactions such as dry reforming of methane (DRM), the reverse water–gas shift reaction (RWGS), or the Boudouard equilibrium need to be considered [10], which makes the reaction network much more complex. Exploiting mechanisms adapted from previous publications, the spatially resolved experimental data obtained herein are compared with simulations in order to determine the model that describes the chemical processes occurring inside the reactor most accurately.

2. Methodology

2.1. Experimental setup and procedure

The experimental setup is based on a high-temperature test facility, which has already been described in previous publications [10–12,18,28,44,52,53], and which was modified for the purpose of this work. Fig. 1 schematically shows the general setup. Argon (Ar), synthetic air, CH_4, CO_2, and H_2 were dosed into the high-temperature reactor by means of mass flow controllers (Bronkhorst). The reactor consisted of a ceramic α-Al_2O_3 tube (DEGUSSIT AL23, Kyocera) with an inner diameter of 20 mm and a length of 1000 mm. Electric heating was used to ensure an isothermal hot zone (~ 400 mm) in the middle of the reactor (Fig. 1b). The reactor tube and heating wires, encased in insulating material, were fixed in a pressure vessel, which ensured the mechanical stability of the ceramic tube at all times, even in the event of a sudden pressure increase, by building up a slight overpressure of 0.2 bar through the supply of Ar. The hot zone temperature was measured outside the ceramic tube, directly on the outer wall of the tube, using a Pt-Rh-based thermocouple. The outer jacket and the connecting flanges were cooled by water.

Spatially resolved gas phase species concentration profiles were measured using fine ceramic tubes (DEGUSSIT AL23, Kyocera) with an inner diameter of 1.6 mm, an outer diameter of 3 mm, and a length of either 1200 mm (for measuring the lower reactor area) or 800 mm (for measuring the upper reactor area), respectively. Note, that only one capillary at the same time was inserted and moved along the tube. The capillary was attached to the gas inlet, where high-temperature-resistant graphite gaskets were used to ensure both a firm attachment to the flange and a movement in vertical direction.

Before the gas stream entered the analyzer, it was passed through a solid filter and a rotameter (Fig. 1a) in order to precisely adjust the volume flow to the analyzer to 25 ml/min, which was less than 5 % of the total volume flow in the reactor. With the aid of a 3-way valve (Fig. 1a), the analytical flow could be directed either into a gas chromatograph (Agilent 6890 N, with ShinCarbon ST column from Restek) or into a mass spectrometer (MS; Hiden Analytical HPR-20 R&D). Regarding data accuracy, the main components (H_2, CH_4, CO, CO_2, and H_2O) were measured with an average deviation of 5 % and the minor components (C_2H_6, C_2H_4, C_2H_2, and C_6H_6) were quantified with an average deviation of 8 %. At the outlet of the reactor there was both a path to the analytics and a path to the exhaust gas line, whereby the gas flow in both could be regulated using needle valves.

Experiments were carried out at 1 bar using either CH_4 or synthetic biogas – a mixture of CH_4:CO_2 with a constant molar CH_4:CO_2 ratio of 2:1 was chosen – as feed gas; H_2 served as carrier gas/diluent and the residence time was set to 5 s. Regarding hydrogen inhibition, two phenomena can occur. On one hand, the presence of H_2 can suppress the formation of hydrocarbon byproducts, leading to slightly higher H_2 selectivities [53]. On the other hand, the presence of H_2 inhibits the pyrolysis reaction [54] with up to 50 % lower CH_4 conversions compared to Argon diluted pyrolysis of methane [53]. Therefore, H_2 dilution can be used to limit soot formation [11], which counteracts possible blockages of the reactor and especially the capillary. In summary, a trade-off between suppressing carbon formation and CH_4 conversion needs to be considered. As the inhibitory effect itself was discussed in a previous study [53], a fixed value of H_2:CH_4 = 2:1 and H_2:biogas = 2:1 was chosen and adapted throughout this work.

The hot zone temperature was varied from 1000 °C to 1400 °C (for CH_4 as feed gas) and from 1000 °C to 1600 °C (for biogas as feed gas) in 100 °C steps. Inside the reactor, a gas sample was obtained through the ceramic capillary every 100 mm and analyzed, which sums up to 11 measurement points in total, with the zero-point representing the upper

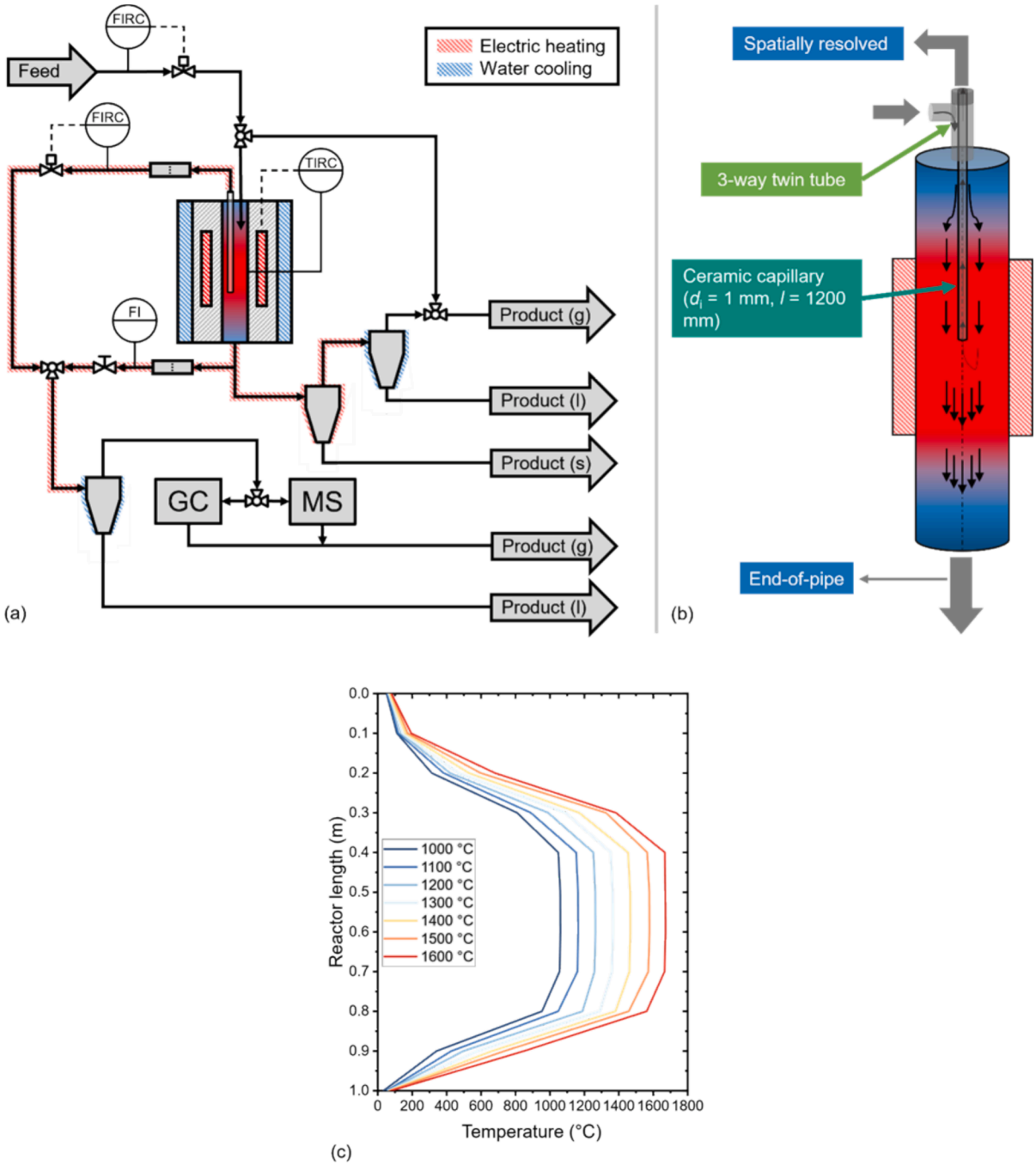

Fig. 1. Basic flow diagram of the experimental setup (a), schematic drawing of the reactor, capillary and heating zone (b), and temperature profiles inside the reactor (c).

end, i.e. the inlet of the reactor.

For each combination of feed gas and temperature, the capillary was positioned first and then the respective H_2-diluted feed gas was fed into the reactor until end-of-pipe stationarity was observed according to the MS data. Subsequently, a gas sample was fed through the capillary and continuously analyzed by MS in order to be able to detect stationarity here as well; then a gas sample was also analyzed by GC. Herein, CH_4, CO_2, CO, and the intermediates acetylene (C_2H_2), ethylene (C_2H_4), ethane (C_2H_6), and propylene (C_3H_6) could be quantified in the gas chromatograph (GC) and the MS. In contrast, benzene (C_6H_6) and H_2 could not be quantified with the GC column used at appropriate retention times and were thus solely analyzed in the mass spectrometer. After the analysis of one axial position inside the reactor, the reactor was flushed with Ar before any carbon deposits in the reactor and in the capillary were burned off using synthetic air. The reactor was then flushed again with Ar and the capillary was repositioned. After any Ar was purged using H_2, the respective feed gas was dosed again and the following axial position was analyzed. Since a spatially resolved quantification of solid carbon formation, i.e. due to deposition reactions and soot formation, cannot be realized experimentally, the amount of formed carbon is discussed in the context of the obtained spatially resolved gas phase data and in particular on the basis of numerical data. Note, that the total quantity of formed solid carbon was already studied in previous studies of our group on methane and biogas pyrolysis [10,18]: using comparable reaction parameters as chosen herein, total carbon yields of more than 90 % could be achieved.

2.2. Modelling

For simulating pyrolysis experiments, a one-dimensional heterogeneous packed-bed reactor model, as implemented in the DETCHEM^{PBR} computer code, was utilized. This model is based on a continuum approach and integrates mass and heat transport with gas phase and surface reactions [55]. A more detailed description of the packed-bed reactor model used herein can be found elsewhere [28,44,56]. In brief, the continuity equation, shown in Equation (1), is used to calculate the mass flux in the reactor system.

$$\frac{\mathrm{d}(\rho u)}{\mathrm{d}z} = P' \sum_{i \in S_g} R_i^{\mathrm{surf}} \tag{1}$$

Herein, ρ is the gas phase mixture density, u is the superficial velocity, z is the axial coordinate, P' is the chemically active perimeter per unit length, S_g is the set of gas phase species, and R_i^{surf} is the effective mass production rate of gas phase species i by surface reactions (in this case, direct carbon deposition reactions on the reactor wall). In addition, the species mass balance is solved according to Equation (2).

$$\rho u \frac{\mathrm{d}Y_i}{\mathrm{d}z} + Y_i P' \sum_{i \in S_g} R_i^{\mathrm{surf}} = P' R_i^{\mathrm{surf}} + R_i^{\mathrm{gas}} \tag{2}$$

Herein, Y_i is the mass fraction of gas phase species i, and R_i^{gas} is the effective mass production rate of gas phase species i by gas phase reactions. It should be noted that the energy balance is not addressed in the current work; instead, the actual experimentally determined temperature profile (Fig. 1c) in the reactor is employed. DETCHEM^{PBR} also includes the capability to simulate soot formation and growth in the reactor [57]. In the current simulations, both soot formation in the gas phase as well as direct carbon deposition on the reactor walls were considered. The appropriate representation of the spatial profiling (SpaciPro) experiment requires the simulations to consider two distinct geometric sections: one corresponding to the capillary used for measurements and the other to the reactor. During the transition from the first section (reactor) to the second (capillary), all the properties were kept unchanged except for the volumetric flow rate. The change in volumetric flow rate between the first section and the second section was determined experimentally and then used for the simulations. A schematic illustration regarding the sections is depicted in Fig. 2.

For the simulations, detailed chemical kinetics were employed. In particular, the gas phase reaction mechanism by Appel et al. [29] (hereinafter referred to as ABF2000, 99 species, 538 reactions) was used for methane pyrolysis. For biogas as the feedstock, in addition to ABF2000, two more gas phase mechanisms were employed: one proposed by Blanquart et al. [58] (Caltechmech, 149 species, 1651 reactions) and the other by Porras et al. [36] (Polymech, 83 species, 558 reactions). To account for the carbon deposition on the reactor wall, the mechanism proposed by Mokashi and Shirsath et al. [28] was coupled with the respective gas phase mechanisms.

3. Results and discussion

The methodology described above allowed to measure the mole fractions of the gas phase as a function of the axial reactor position (with 0 m representing the reactor entrance) and to compare the experimental results with modelled data. The experiments were carried out at constant atmospheric pressure, a residence time of 5 s and a molar H_2:feed gas (CH_4 or biogas) dilution ratio of 2:1, while the temperature was varied. The results for methane (at 1000 °C, 1200 °C, and 1400 °C) and for biogas (consisting of CH_4 and CO_2 with a molar CH_4:CO_2 ratio of 2:1 at 1000 °C, 1200 °C, and 1400 °C) as feed gas are presented below. The results at 1100 °C, 1300 °C, 1500 °C, and 1600 °C are shown in the SI.

3.1. Methane as feedstock

Fig. 3 shows the steady-state gas phase composition inside the reactor as a function of the axial position at a temperature of 1000 °C with CH_4 as feed gas. At a temperature of 1000 °C, the thermal decomposition reaction is kinetically controlled at the applied residence time (5 s), resulting in an only marginal change in the CH_4 and H_2 proportions (Fig. 3a). This is consistent with previous end-of-pipe results reported in literature [10–12]. In contrast, spatially resolved profiles of the minor species (Fig. 3b and Fig. 3c) provide important insights into the mechanistic processes in the gas phase. For instance, around a reactor position of 0.2 m, the formation of C_2H_6 can be observed, which is believed to form by recombination of methyl radicals [12,34]. C_2H_6 is ultimately dehydrogenated to C_2H_4, whereby the latter can be observed from a reactor position of 0.4 m and reaches a peak mole fraction of 0.0018 at 0.8 m, after which it is converted almost completely at the end of the reactor. Thus, C_2H_2 is formed by further dehydrogenation, which can be observed experimentally from a position of 0.6 m and reaches a peak mole fraction of 0.0005 at a position of 0.7 m. C_6H_6 forms as well from this position onwards, mainly *via* the recombination of C_3H_3 radicals [30,44,59], but in much smaller quantities compared to the other byproducts. Overall, at a hot zone temperature of 1000 °C the experimental results show the formation of C_2H_2 and C_2H_4 species, which are primarily responsible for the formation of solid carbon on the reactor wall [28,32,33].

Numerical simulations are in fairly good agreement with the

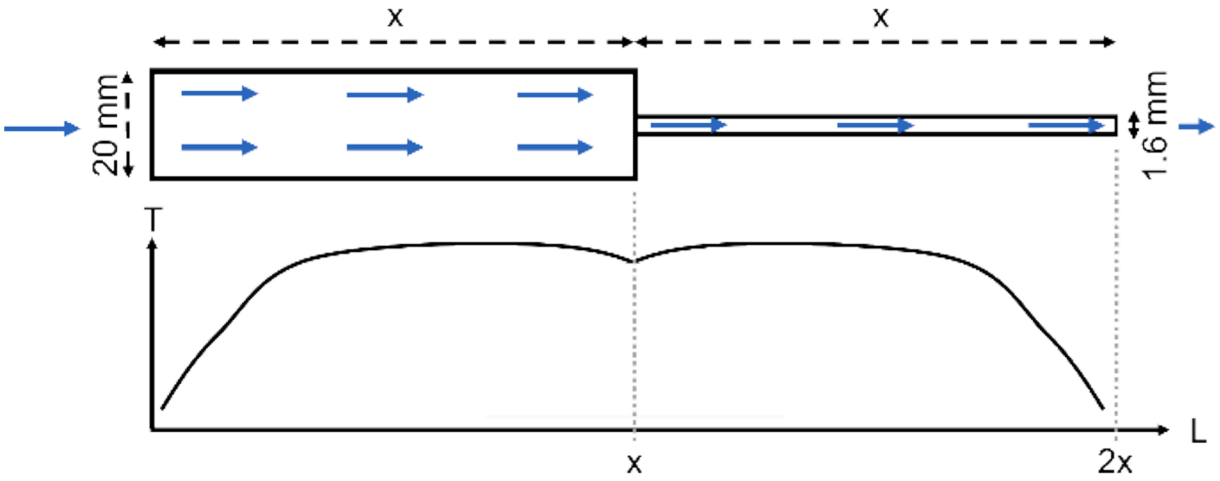

Fig. 2. Schematic illustration of the temperature profile and volumetric flow rate used for the numerical simulations. x represents the position of the capillary inside the reactor.

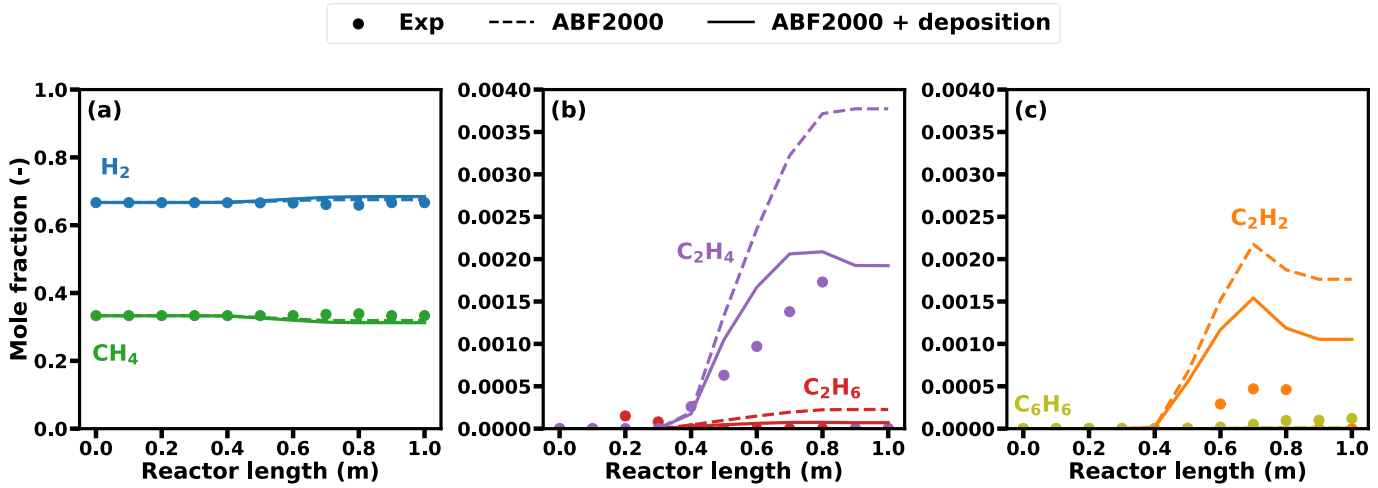

Fig. 3. Spatially resolved gas phase composition as a function of reactor length at a pressure of 1 bar, a residence time of 5 s, a molar H_2:CH_4 dilution of 2:1 and a temperature of 1000 °C.

experimental data for H_2 and CH_4 (Fig. 3a). However, the mole fractions of the byproducts, C_2H_4 and C_2H_2, are consistently overpredicted (Fig. 3b, Fig. 3c). The comparison of experimental and numerical data shows that the gas phase microkinetic model, ABF2000, (dashed lines in Fig. 3) alone is insufficient to describe the pyrolysis reaction. Therefore, another set of simulations were performed accounting for direct carbon deposition reactions on the reactor wall (solid lines in Fig. 3), leading to a better agreement with the experimental results, especially for minor species. These deposition reactions comprise mainly the decomposition of C_2, C_4, and C_6 species; their deposition leads to a lower total amount of carbon in the gas phase. Although the simulation trends align well with experimental data, relative deviations of up to 30 % are observed, which can be attributed to the slower reaction rate of the deposition reactions [28,57] compared to experimentally observed results. The present results are in line with previous studies [28,57], which showed deviations for minor species at a lower hot zone temperature (< 1000 °C). Since temperatures of well above 1000 °C are required to achieve technically relevant CH_4 conversions, the spatially resolved gas phase composition at a temperature of 1200 °C is shown in Fig. 4.

A significant increase in the H_2 mole fraction from 0.66 to over 0.85 and a simultaneous decrease in the CH_4 fraction from 0.34 to approx. 0.10 can be observed experimentally, with both starting in front of the hot zone of the reactor (0.3 m) (Fig. 4a). At this position, the temperature is sufficiently high to overcome the kinetic barrier. As the hot zone temperature increases from 1000 °C to 1200 °C, neither C_2H_6 nor C_6H_6 can be observed in relevant amounts, which indicates higher decomposition rates to form solid carbon (Fig. 4b and Fig. 4c) [28,57]. Experimentally, it can be observed that within the first few mm of the hot zone, mole fractions of C_2H_4 and C_2H_2 are peaking with 0.01 and 0.015, respectively. Along the reactor length, both species are partly consumed, presumably during the formation of higher hydrocarbons and solid carbon on the reactor wall, as suggested by the simulations taking carbon surface kinetics into account [28]. However, the formation of C_6H_6 is overestimated, which can be attributed to the soot formation model that currently assumes pyrene dimers as proxy species for soot nucleation instead of C_6H_6 and PAHs [57]. Additionally, the overprediction could be related to a too low deposition reaction rate of C_6H_6, overestimating soot formation in the reactor. For further clarification, more studies in this direction are needed. In general, it can be observed that with an increasing hot zone temperature the numerical results considering deposition reactions align better with the experimental results.

Further increasing the hot zone temperature to 1400 °C leads to almost full CH_4 conversion at the reactor outlet (Fig. 5a) with over 90 % conversion taking place in one third of the initial hot zone of the reactor. Among the byproducts, only C_2H_4 (Fig. 5b) and C_2H_2 (Fig. 5c) are

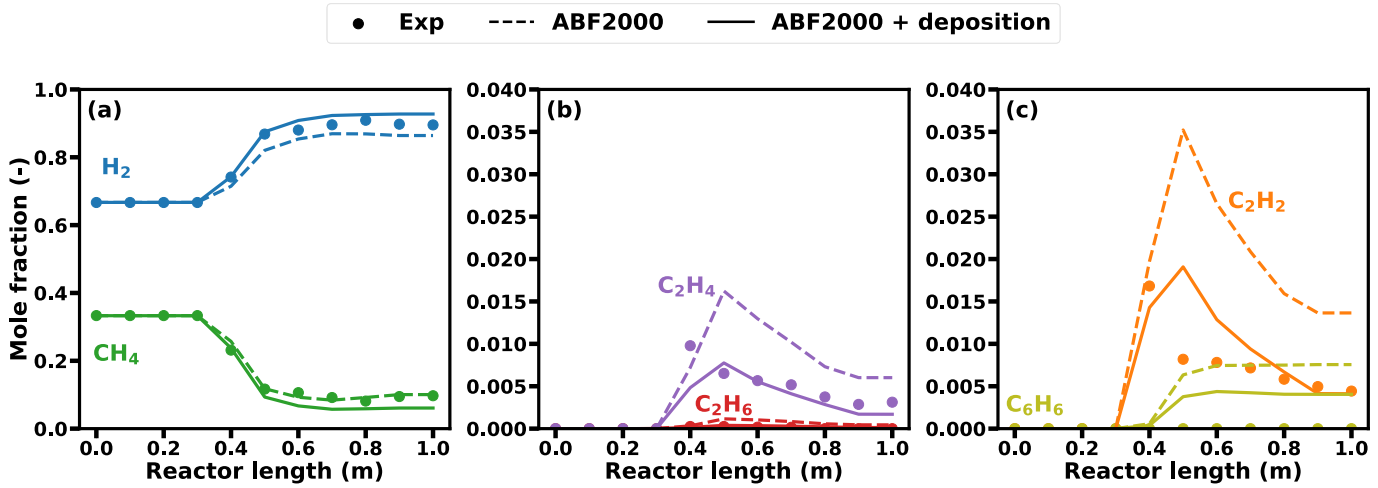

Fig. 4. Spatially resolved gas phase composition as a function of reactor length at a pressure of 1 bar, a residence time of 5 s, a molar H_2:CH_4 dilution of 2:1 and a temperature of 1200 °C.

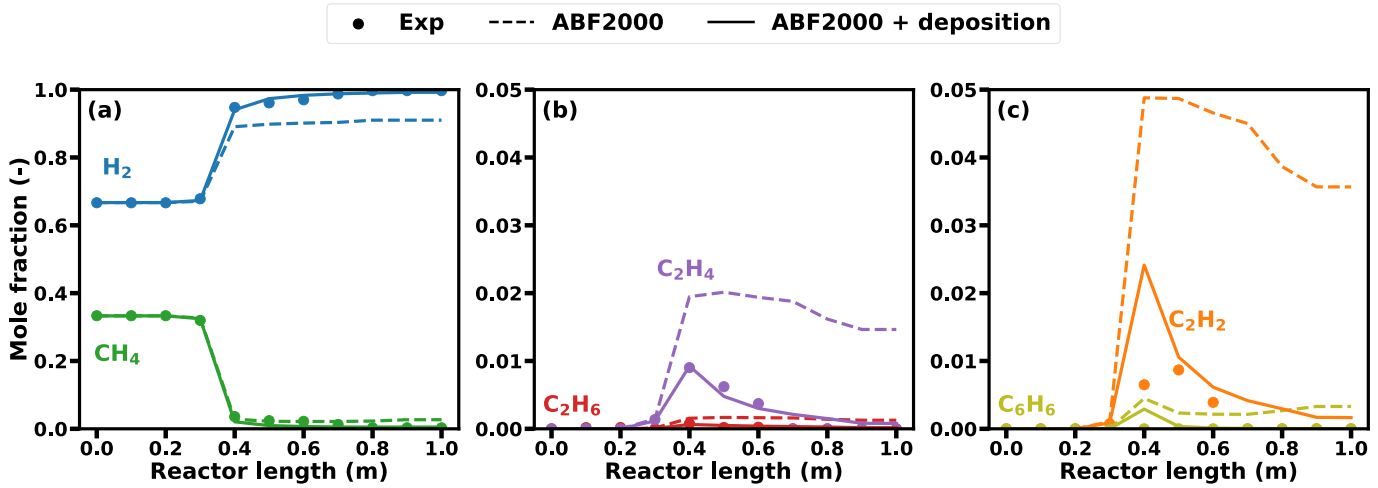

Fig. 5. Spatially resolved gas phase composition as a function of reactor length at a pressure of 1 bar, a residence time of 5 s, a molar H_2:CH_4 dilution of 2:1 and a temperature of 1400 °C.

present in relevant quantities with a peak mole fraction of 0.01 for both at a reactor position of approx. 0.4 m. Compared to a hot zone temperature of 1000 °C and 1200 °C (Fig. 3 and Fig. 4), the experimental results show that the peak of the byproduct mole fraction shifts towards the entrance of the reactor, most likely because the reaction rates increase with the increasing hot zone temperature. This trend, too, is correctly captured by the simulations taking carbon deposition reactions into account. In contrast to the findings with a hot zone temperature of 1200 °C (Fig. 4), both C_2H_4 (Fig. 5b) and C_2H_2 (Fig. 5c) are almost fully converted within the hot zone of the reactor, which can be attributed to the higher carbon deposition (decomposition of C_2 and C_6 species) on the reactor wall of the hot zone region [28]. Furthermore, experimentally C_6H_6 was found only in negligible quantity, whereas the simulations predict a mole fraction of up to 0.005 in the hot zone of the reactor (Fig. 5c). Additionally, the numerical model also predicts the formation of PAHs [44,57], which are responsible for soot formation. Notably, in addition to the deposition on the reactor wall, also the formation of soot was observed during the experimental measurement campaign. Therefore, both experimentally and numerically, two simultaneous carbon formation pathways were confirmed, namely the decomposition of C_2 and C_6 species to form solid carbon on the reactor wall and the formation of soot *via* PAHs. That the numerical simulations suggest a higher relevance of carbon deposition reactions compared to soot formation [28,57] is in line with the experimentally observed immediate consumption of C_6H_6 over the reactor length.

3.2. Biogas as feedstock

When biogas – mainly a mixture of CH_4 and CO_2 – is fed into a high-temperature reactor instead of CH_4, further reactions such as dry reforming, reverse water–gas shift or the Boudouard equilibrium must be considered [10]. In order to investigate the extent to which these reactions evolve, spatially resolved gas phase compositions are essential. Therefore, Fig. 6 shows the gas phase composition inside the reactor as a function of the axial position at a temperature of 1000 °C if biogas is used as feed gas.

For a biogas feed, in addition to H_2 and hydrocarbons, also CO (Fig. 6a) and H_2O (Fig. 6b) can be observed as products. At a hot zone temperature of 1000 °C, a minor conversion of H_2, CH_4 (Fig. 6a), and CO_2 (Fig. 6b) can be observed starting from the hot zone of the reactor. CO and H_2O are formed in the same area, each with a mole fraction of up to approx. 0.04. Herein, the formation of CO takes place *via* dry reforming (Eq. (3)), reverse water–gas shift (Eq. (4)), and *via* the Boudouard equilibrium (Eq. (5)).

$$CH_4 + CO_2 \rightleftharpoons 2CO + 2H_2 \; ; \; 247 \text{ kJ/mol} \tag{3}$$

$$CO_2 + H_2 \rightleftharpoons CO + H_2O \; ; \; 41 \text{ kJ/mol} \tag{4}$$

$$CO_2 + C \rightleftharpoons 2CO \; ; \; 172 \text{ kJ/mol} \tag{5}$$

For all of the above-mentioned reactions that consume CO_2, the equilibrium at the reaction temperatures considered in this work lies on the side of CO [60–62], with the mole fraction of the latter increasing over the reactor length. Moreover, the formation of H_2O can only be explained by the RWGS reaction. In line with previous studies [63], the RWGS reaction plays a key role at lower hot zone temperatures, resulting in the consumption of H_2 and the formation of CO and H_2O. While C_2H_6 (Fig. 6c), C_2H_2, and C_6H_6 (Fig. 6d) do not form in significant

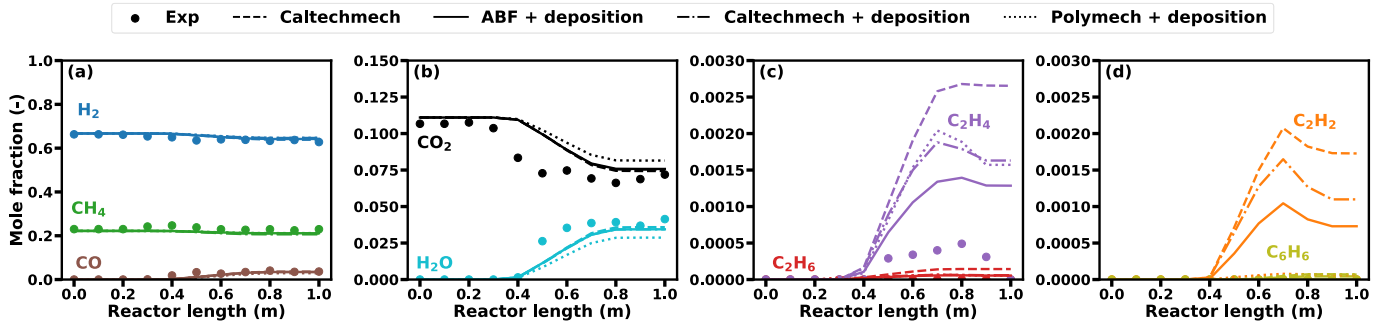

Fig. 6. Spatially resolved gas phase composition as a function of reactor length at a pressure of 1 bar, a residence time of 5 s, a molar H_2:CH_4 dilution of 2:1, a molar CH_4:CO_2 ratio of 2:1 and a temperature of 1000 °C.

amounts, small amounts of C_2H_4 can be observed with mole fractions of less than 0.001 (Fig. 6c). This value is in the same order of magnitude as that observed in the case of a pure methane feed at 1000 °C (Fig. 3b, approx. 0.0015), indicating that the addition of CO_2 to the feed leads to additional side reactions, but does not majorly affect the conventional pyrolysis route *via* C_2, C_4, and C_6 species at 1000 °C. Consequently, the comparatively lower proportions of hydrocarbons in comparison to the pure methane feed can be attributed to the lower absolute amount of methane in the biogas feed [10].

Fig. 6 also shows the numerical results that were obtained when using different kinetic models. For the major gas phase species H_2, CH_4, CO_2, CO, and H_2O the description of the experimentally observed trends is fairly good. Although all kinetic models are able to capture the overall trends regarding the gas phase species concentrations during biogas pyrolysis, the model coupling the ABF2000 mechanism with deposition reactions provides the most accurate results. The most pronounced deviations, both among the models and compared to the experimental data, are obtained for the minor species (C_2H_6, C_2H_4, C_2H_2, and C_6H_6 (Fig. 6c, d): At lower temperatures, the simulations overpredict the byproduct levels, similar to what was found for CH_4 pyrolysis at 1000 °C (Fig. 3).

The spatially resolved species concentration profiles depicted in Fig. 7 reveal the interplay between CH_4 pyrolysis, dry reforming, and the RWGS reaction at a hot zone temperature of 1200 °C. The results reveal significant CH_4 conversion, with residual CH_4 mole fractions of approx. 0.08 and almost full CO_2 conversion within the reactor (Fig. 7a and Fig. 7b). With a mole fraction of ~ 0.1, CO is formed as a primary product and also significant H_2 production is observed (plateau of ~ 0.73 near the reactor outlet).

A clear difference to a hot zone temperature of 1000 °C (Fig. 6) can be seen in the H_2, CO, and H_2O mole fractions. Herein, H_2 exhibits a minimum right in front of the hot zone, but rapidly increases afterwards and finally results in net H_2 production at the reactor outlet. Furthermore, H_2O formation is observed upon the onset of feed gas species conversion. A critical observation is the distinct local maxima in H_2O and CO mole fractions at approx. 0.5 m that indicate the transition from RWGS dominance in front of the hot zone to dry reforming and pyrolysis dominance in the hot zone. This transition emphasizes the critical role of temperature in governing reaction regimes: while the RWGS reaction promotes H_2O and CO formation at lower temperatures, CH_4 reforming and pyrolysis reactions dominate once the hot zone temperature stabilizes [63]. This ultimately increases the net production rate of H_2 compared to lower temperatures, which finally reaches a plateau at a molar fraction of about 0.73.

Moreover, the formation of C_2H_4 (Fig. 7c), C_2H_2, and C_6H_6 (both Fig. 7d) is noteworthy. Their profiles peak at approx. 0.5 m, coinciding with the temperature ramp in the reactor. Among these, C_2H_2 reaches the highest mole fraction (~ 0.01), which underscores its role as a key intermediate in carbon deposition reactions [28,29,39]. The diminishing C_2H_4 and C_6H_6 mole fractions towards the reactor outlet suggest their consumption in secondary reactions, including surface deposition and further pyrolysis. Compared to the data reported for a hot zone temperature of 1000 °C (Fig. 6), reaction kinetics are accelerated at 1200 °C, enhancing both CH_4 and CO_2 conversion, and shifting the maxima of the hydrocarbon intermediates closer to the hot zone. This aligns with the expected behavior of temperature-sensitive reactions like CH_4 pyrolysis and dry reforming [11,63,64]. This observation allows for a more detailed breakdown of the different reaction zones: After the RWGS-dominated regime near the entrance of the hot zone, dry reforming appears to dominate in the subsequent zone, followed by pyrolysis, which gradually becomes more pronounced as soon as the isothermal zone is reached [63].

In analogy to the interpretation of the data with the CH_4 feed, the agreement between experiments and simulations improves for higher hot zone temperatures and associated higher conversions. The Caltech mechanism, when coupled with carbon deposition reactions, demonstrates higher predictive accuracy compared to the ABF2000 mechanism. This can be attributed to the comprehensive nature of the Caltech mechanism, which includes detailed reaction pathways for small hydrocarbons, intermediate species (e.g., C_3H_6), and precursors to soot and PAHs [58,63]. These features allow to capture the interplay between gas phase reactions and surface deposition dynamics more accurately compared to the ABF2000 mechanism. The latter, while computationally efficient and adequate for CH_4 combustion and pyrolysis, lacks intermediate species like C_3H_6 and detailed pathways for larger hydrocarbons [12,29]. Furthermore, the overestimation of the H_2O content in the product gas (Fig. 7b) suggests potential limitations in the RWGS kinetic parameters within the ABF2000 model. This discrepancy could be addressed by refining the RWGS kinetics or by incorporating more advanced thermodynamic data.

A further increase of the hot zone temperature to 1400 °C (Fig. 8) shifts the reaction regime further, with pyrolysis and dry reforming becoming more dominant. Unlike at 1200 °C (Fig. 7), the profiles exhibit a reduced or even absent local minimum for H_2 and local maximum for CO, indicating smoother reaction progressions (Fig. 8a). However, H_2O retains a local maximum of ~ 0.05 at approx. 0.4 m, highlighting the diminishing but still relevant role of the RWGS reaction in the initial hot zone. The significantly lower H_2O content compared to a hot zone temperature of 1200 °C (Fig. 7) underscores the temperature-driven reduction in RWGS contribution and increased CH_4 pyrolysis efficiency. The residual H_2O at the reactor outlet (with a mole fraction of approx. ~ 0.02) suggests potential for further optimization through increased reactor temperatures or longer residence times. For instance, at 1600 °C (shown in the SI), minimal quantities of H_2O can be obtained at the reactor outlet.

Furthermore, CO_2 and CH_4 are both almost fully converted, leading to CO formation and contributing to both H_2 production and solid carbon deposition. The interplay between C-C coupling reactions and the formation of C_2H_2 – a key intermediate in carbon deposition – becomes particularly evident at 1400 °C. The persistence of C_2H_2 and C_2H_4

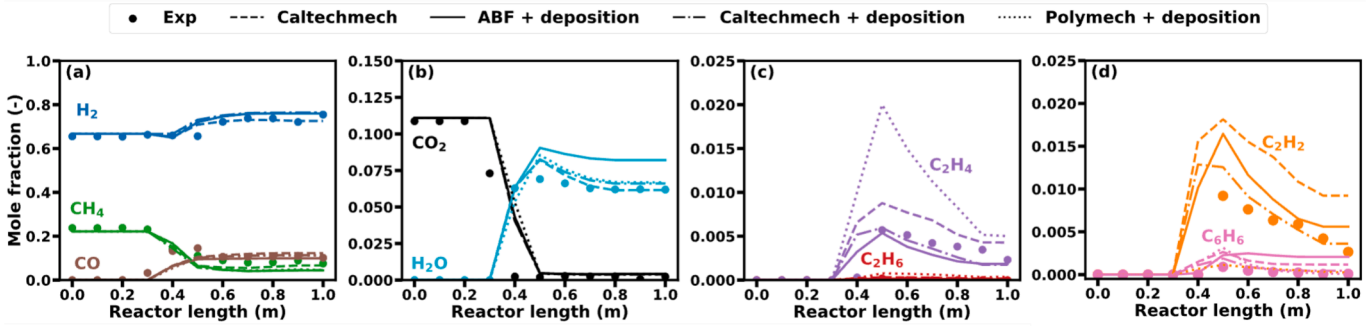

Fig. 7. Spatially resolved gas phase composition as a function of reactor length at a pressure of 1 bar, a residence time of 5 s, a molar H_2:CH_4 dilution of 2:1, a molar CH_4:CO_2 ratio of 2:1 and a temperature of 1200 °C.

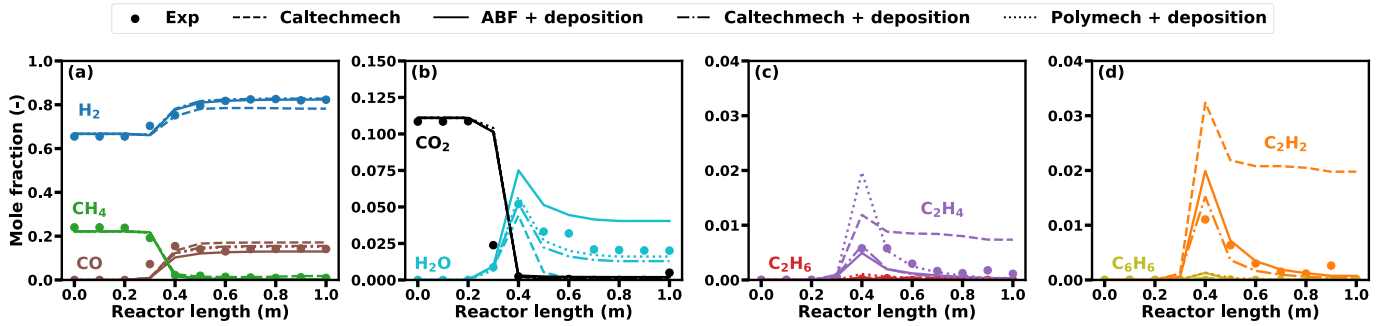

Fig. 8. Spatially resolved gas phase composition as a function of reactor length at a pressure of 1 bar, a residence time of 5 s, a molar H_2:CH_4 dilution of 2:1, a molar CH_4:CO_2 ratio of 2:1 and a temperature of 1400 °C.

despite the higher reaction temperatures underlines their critical role as intermediates in both gas phase and deposition reactions. The simulations accurately predict their behavior, with peaks at approx. 0.4 m and reduced outlet mole fractions due to consumption in secondary reactions.

3.3. Translation of spatial insights into industrial considerations

The spatially resolved results on methane and biogas pyrolysis discussed above provide important insights that are a prerequisite for industrial reactor design. Suppressing the formation of undesired byproducts in the gas phase and maximizing the methane decomposition efficiency is essential in order to achieve sufficient hydrogen yields for both feed gases.

Herein, one important measure that should be taken into account during industrial reactor design is the introduction of a carbon bed, which can have a significant impact on CH_4 conversion and product composition. For instance, if solid carbon is used as bed (fixed bed, moving bed or fluidized bed) inside the reactor, increased conversions and selectivities can be observed compared to identical reaction conditions in an empty tube setup. This was already demonstrated with end-of-pipe results in previous publications of our group [10,18]. With regard to the reaction regimes identified in our present study by means of spatial profiling, the presence of solid carbon accelerates the pyrolysis and dry reforming reactions as well as deposition processes [10,18] and therefore leads to a faster reaction of the intermediates. Their faster consumption during the accelerated reactions in reactor configurations containing a carbon particle bed makes the reaction regimes discussed above more compact and thus offers the chance for higher throughput, provided that the residence time is adjusted precisely: It should be as low as possible to ensure a high throughput, but also high enough to ensure sufficiently high methane and carbon dioxide conversion and, above all, a complete reaction of the intermediates within the reactor. The latter can also be achieved, for example, by adjusting the temperature profile within the reactor. The experimental setup used in our work has a heating and cooling zone (c.f. Fig. 1), which is not optimal for suppressing byproduct formation on the one hand, but allows for detailed investigations on kinetics on the other hand. Consequently, such a setup geometry is beneficial primarily for academic purposes. In terms of upscaling, a heat-integrated system can be set up through faster heating, a homogeneous temperature profile, and a downstream quenching system, in which the formation of byproducts, both gaseous and PAH, can be minimized. The aspects of throughput and product purity are of major economic importance, as they strongly govern the setup capacity and may make complex and expensive effluent gas stream purification measures redundant.

Furthermore, the results presented herein can be used to validate reactor models. In this work, we focused on validation of mechanisms that were applied in recent studies on methane and biogas pyrolysis [28,63] especially at temperatures above 1200 °C; herewith, reactor design by means of reliable numerical simulations and kinetic models is facilitated. In order to account for the deviations between experimental and simulated data especially in the low-temperature regime, adjustments of the deposition reaction rates would quantitatively reduce the predicted concentrations of minor species by enhancing their conversion into solid carbon, thus improving the agreement with experimental data. Results from previous studies of our group [28,57] suggest that increasing the deposition rates can lower the mole fractions of C_2H_2 and C_2H_4 by 10 % to 15 %, which could be a feasible approach to address their overprediction in the model. While within this study sensitivity analyses have been conducted only indirectly by comparing models with and without deposition reactions, demonstrating their strong influence on minor species, a comprehensive systematic parametric sensitivity study (e.g., varying deposition rates by ± 50 %) could further refine the model. Notably, this workflow is not limited to the models used herein, but may also be exploited for validation and improvement of other kinetic models such as NUIGMech: This mechanism was originally developed for combustion applications and therefore captures also oxidation and flame propagation [65], but it was also used in a reduced version for methane pyrolysis [66]. A future study could benchmark this mechanism against the ones employed in this study, in particular to assess its suitability for non-oxidative dry reforming and pyrolysis-dominated regimes. Including further experimental evidence on the decomposition mechanism, e.g. from *in situ* methods such as laser absorption spectroscopy [67], would allow for further validation of the models. However, reactor configurations suitable for such laser-based analyses call for optical accessibility and unique reactor geometries, which makes conditions frequently less comparable to industrial processes. In contrast, the high-temperature flow reactor used within this work enables operation under industrially relevant conditions. Thus, the present study, which was carried out in the same experimental setup as employed in previous studies of our group including both experiments and numerical models [10,11,18,28,53,57,63] under similar conditions, solely with the modification of the ceramic capillary unit, joins the latter corpus of work: It ensures comparability of the results to previous studies and provides direct spatially resolved insights into reactor operation under industrially feasible conditions.

4. Conclusions

Within this work, experimentally determined and numerically predicted axial concentration profiles were studied in the context of thermal methane and biogas pyrolysis. Microkinetic models such as the ABF2000 mechanism [29], which was originally developed for describing soot formation in laminar premixed flames of C_2 hydrocarbons and which is, in adapted form, frequently used to describe the pyrolysis of methane [28], were used in the simulations. Spatially resolved concentration profiles of the main components (H_2, CH_4, CO, CO_2, and H_2O) as well as for minor components (C_2H_6, C_2H_4, C_2H_2, and C_6H_6) were reported.

Solely relying on gas phase kinetics allowed to only partly predict the

measured gas phase profiles. Considering also direct deposition reactions of C_2 species and soot formation *via* the C_6H_6-PAH route results in a fairly good agreement between simulations and experiments. In particular, the ABF2000 mechanism coupled with a previously proposed deposition model [28] could capture the experimental trends sufficiently, especially for hot zone temperatures above 1200 °C. For lower temperatures, however, the minor components are overpredicted by the simulations, which is attributed to lower reaction rates of the deposition reactions within the model compared to experimentally observed results. To achieve satisfying agreement between simulations and experiments, the rates of heterogeneous reactions at lower temperatures (< 1200 °C) should be adapted. Discrepancies remain for C_6H_6, both with respect to spatially resolved data as well as end-of-pipe data. This deficiency may be interpreted by an imbalance between the soot formation rate and the carbon formation rate by deposition, in which the deposition reactions are underestimated.

If biogas is used as an entirely renewable feedstock, not only the conventional pyrolysis route, but also other reactions such as dry reforming, reverse water–gas shift, and the Boudouard equilibrium must be taken into account. These reactions produce a gas mixture with H_2 and CO as main product gases, which could be used as syngas for further process steps. Herein, the spatially resolved measurements allowed to identify different reaction regimes that clearly correlate with the temperature profile within the reactor: While the RWGS reaction, which consumes CO_2 and H_2 and produces CO and H_2O, dominates between the reactor inlet and the isothermal hot zone, dry reforming (endothermic CH_4 and CO_2 conversion to CO and H_2) dominates the subsequent zone. Consecutively, pyrolysis becomes relevant once a sufficiently high temperature is reached in the isothermal hot zone. These regimes shift with temperature, highlighting the importance of precise thermal control – e.g. by using a heat-integrated system with a short heating zone, a homogeneous temperature profile in the hot zone, and a downstream quenching system – for optimizing syngas quality and minimizing the formation of byproducts.

In addition, the same intermediates, i.e., light hydrocarbons and C_6H_6, that were already observed during experiments with methane as the feed gas, can also be detected with a biogas feed. The Caltech mechanism [58] coupled with direct carbon deposition reactions [28] stands out due to its high accuracy in predicting the intricate reaction network during biogas pyrolysis over a wide temperature range. Overall, the results presented in the present work can serve as a basis for future numerical studies on thermal methane and biogas pyrolysis, providing valuable data for fine tuning of the respective deposition models.

Funding sources

Not applicable.

CRediT authorship contribution statement

Ahmet Çelik: Writing – original draft, Visualization, Validation, Methodology, Investigation, Formal analysis, Data curation, Conceptualization. **Akash Bhimrao Shirsath:** Writing – original draft, Investigation, Formal analysis. **Manas Mokashi:** Investigation, Formal analysis. **Jonas Tatzig:** Investigation, Formal analysis. **Heinz Müller:** Investigation, Formal analysis. **Olaf Deutschmann:** Writing – review & editing, Supervision, Resources, Project administration, Conceptualization. **Patrick Lott:** Writing – original draft, Supervision, Resources, Project administration, Data curation, Conceptualization.

Declaration of competing interest

The authors declare that they have no known competing financial interests or personal relationships that could have appeared to influence the work reported in this paper.

Acknowledgements

We thank Berg-idl GmbH for their support in engineering the high-temperature vessel of the experimental setup, and S. Lichtenberg (KIT) for technical support.

Appendix A. Supplementary data

Supplementary data to this article can be found online at https://doi.org/10.1016/j.cej.2025.163167.

Data availability

All data analyzed can be found in the article and the supplementary material..

References

[1] Z. Liu, Z. Deng, S.J. Davis, P. Ciais, *Nat. Rev. Earth Environ.* 5 (2024) 253–254.
[2] F. Dawood, M. Anda, G.M. Shafiullah, *Int. J. Hydrogen Energy* 45 (2020) 3847–3869.
[3] J. Dufour, D.P. Serrano, J.L. Gálvez, J. Moreno, C. García, *Int. J. Hydrogen Energy* 34 (2009) 1370–1376.
[4] O. Machhammer, A. Bode, W. Hormuth, *Chem. Eng. Technol.* 39 (2016) 1185–1193.
[5] N. Sánchez-Bastardo, R. Schlögl, H. Ruland, *Ind. Eng. Chem. Res.* 60 (2021) 11855–11881.
[6] S.R. Patlolla, K. Katsu, A. Sharafian, K. Wei, O.E. Herrera, W. Mérida, *Renew. Sustain. Energy Rev.* 181 (2023) 113323.
[7] N. Muradov, T. Veziroğlu, *Int. J. Hydrogen Energy* 30 (2005) 225–237.
[8] A. Çelik, I. Ben Othman, Y. Neudeck, O. Deutschmann, P. Lott, *Energy Convers. Manage.* 326 (2025) 119414.
[9] A. Rafiee, K.R. Khalilpour, J. Prest, I. Skryabin, *Biomass Bioenergy* 144 (2021) 105935.
[10] A. Çelik, I. Ben Othman, H. Müller, P. Lott, O. Deutschmann, *React. Chem. Eng.* 9 (2024) 108–118.
[11] P. Lott, M.B. Mokashi, H. Müller, D.J. Heitlinger, S. Lichtenberg, A.B. Shirsath, C. Janzer, S. Tischer, L. Maier, O. Deutschmann, ChemSusChem 16 (2023) e202201720.
[12] M. Mokashi, A.B. Shirsath, P. Lott, H. Müller, S. Tischer, L. Maier, O. Deutschmann, *Chem. Eng. J.* 479 (2024) 147556.
[13] T. Keipi, K.E.S. Tolvanen, H. Tolvanen, J. Konttinen, *Energy Convers. Manage.* 126 (2016) 923–934.
[14] S.H. Sharif Zein, A.R. Mohamed, P.S. Talpa Sai, *Ind. Eng. Chem. Res.* 43 (2004) 4864–4870.
[15] N. Muradov, *Energy Fuels* 12 (1998) 41–48.
[16] N. Muradov, *Catal. Commun.* 2 (2001) 89–94.
[17] D.P. Serrano, J.A. Botas, R. Guil-Lopez, *Int. J. Hydrogen Energy* 34 (2009) 4488–4494.
[18] A. Çelik, I. Ben Othman, H. Müller, O. Deutschmann, P. Lott, *Discover, Chem. Eng.* 4 (2024) 29.
[19] A. Abánades, E. Ruiz, E.M. Ferruelo, F. Hernández, A. Cabanillas, J.M. Martínez-Val, J.A. Rubio, C. López, R. Gavela, G. Barrera, C. Rubbia, D. Salmieri, E. Rodilla, D. Gutiérrez, *Int. J. Hydrogen Energy* 36 (2011) 12877–12886.
[20] N. Muradov, F. Smith, C. Huang, A. T-Raissi, *Catal. Today* 116 (2006) 281–288.
[21] V. Shilapuram, N. Ozalp, M. Oschatz, L. Borchardt, S. Kaskel, *Carbon* 67 (2014) 377–389.
[22] F. Kerscher, A. Stary, S. Gleis, A. Ulrich, H. Klein, H. Spliethoff, *Int. J. Hydrogen Energy* 46 (2021) 19897–19912.
[23] L. Fulcheri, N. Probst, G. Flamant, F. Fabry, E. Grivei, X. Bourrat, *Carbon* 40 (2002) 169–176.
[24] T. Geißler, M. Plevan, A. Abánades, A. Heinzel, K. Mehravaran, R.K. Rathnam, C. Rubbia, D. Salmieri, L. Stoppel, S. Stückrad, A. Weisenburger, H. Wenninger, T. Wetzel, *Int. J. Hydrogen Energy* 40 (2015) 14134–14146.
[25] D. Kang, N. Rahimi, M.J. Gordon, H. Metiu, E.W. McFarland, *Appl. Catal., B* 254 (2019) 659–666.
[26] M. Dadsetan, M.F. Khan, M. Salakhi, E.R. Bobicki, M.J. Thomson, *Int. J. Hydrogen Energy* 48 (2023) 14565–14576.
[27] N. Muradov, *Int. J. Hydrogen Energy* 26 (2001) 1165–1175.
[28] M. Mokashi, A.B. Shirsath, A. Çelik, P. Lott, H. Müller, S. Tischer, L. Maier, J. Bode, D. Schlereth, F. Scheiff, D. Flick, M. Bender, K. Ehrhardt, O. Deutschmann, *Chem. Eng. J.* 485 (2024) 149684.
[29] J. Appel, H. Bockhorn, M. Frenklach, *Combust. Flame* 121 (2000) 122–136.
[30] M. Frenklach, *Phys. Chem. Chem. Phys.* 4 (2002) 2028–2037.
[31] K. Norinaga, O. Deutschmann, *Ind. Eng. Chem. Res.* 46 (2007) 3547–3557.
[32] K. Norinaga, O. Deutschmann, N. Saegusa, J.-I. Hayashi, *J. Anal. Appl. Pyrolysis* 86 (2009) 148–160.
[33] K. Norinaga, V.M. Janardhanan, O. Deutschmann, *Int. J. Chem. Kinet.* 40 (2008) 199–208.
[34] F. Billaud, C. Gueret, J. Weill, Thermochim. Acta 211 (1992) 303–322.
[35] V. I. Golovitchev, F. Tao, J. Chomiak, SAE Technical Paper (1999) 1999-01-3552.

[36] S. Porras, D. Kaczmarek, J. Herzler, S. Drost, M. Werler, T. Kasper, M. Fikri, R. Schießl, B. Atakan, C. Schulz, U. Maas, *Combust. Flame* 212 (2020) 107–122.
[37] M. Frenklach, H. Wang, *Symp. (int.) Combust.* 23 (1991) 1559–1566.
[38] J.Z. Wen, M.J. Thomson, S.H. Park, S.N. Rogak, M.F. Lightstone, *Proc. Combust. Inst.* 30 (2005) 1477–1484.
[39] A. Li, K. Norinaga, W. Zhang, O. Deutschmann, *Compos. Sci. Technol.* 68 (2008) 1097–1104.
[40] A. Li, O. Deutschmann, *Chem. Eng. Sci.* 62 (2007) 4976–4982.
[41] A. Becker, K.J. Hüttinger, *Carbon* 36 (1998) 177–199.
[42] A. Becker, K.J. Hüttinger, *Carbon* 36 (1998) 201–211.
[43] K.J. Hüttinger, *Chem. Vap. Deposition* 4 (1998) 151–158.
[44] A.B. Shirsath, M. Mokashi, P. Lott, H. Müller, R. Pashminehazar, T. Sheppard, S. Tischer, L. Maier, J.-D. Grunwaldt, O. Deutschmann, *J. Phys. Chem. A* 127 (2023) 2136–2147.
[45] A.B. Shirsath, M.L. Schulte, B. Kreitz, S. Tischer, J.-D. Grunwaldt, O. Deutschmann, *Chem. Eng. J.* 469 (2023) 143847.
[46] J. Kopyscinski, T.J. Schildhauer, F. Vogel, S.M.A. Biollaz, A. Wokaun, *J. Catal.* 271 (2010) 262–279.
[47] O. Korup, S. Mavlyankariev, M. Geske, C.F. Goldsmith, R. Horn, *Chem. Eng. Process.* 50 (2011) 998–1009.
[48] J. Zetterberg, S. Blomberg, J. Gustafson, J. Evertsson, J. Zhou, E.C. Adams, P.-A. Carlsson, M. Aldén, E. Lundgren, *Nat. Commun.* 6 (2015) 7076.
[49] K. Morgan, J. Touitou, J.-S. Choi, C. Coney, C. Hardacre, J.A. Pihl, C.E. Stere, M.-Y. Kim, C. Stewart, A. Goguet, W.P. Partridge, *ACS Catal.* 6 (2016) 1356–1381.
[50] P.-Y. Peng, H. Nguyen, M.P. Harold, D. Luss, in: A.G. Dixon, O. Deutschmann (Eds.), Advances in Chemical Engineering, Academic Press, 2017.
[51] K. Keller, D. Hodonj, L. Zeh, L. Caulfield, E. Sauter, C. Wöll, O. Deutschmann, P. Lott, *Catal. Sci. Technol.* 14 (2024) 4142–4153.
[52] S.D. Angeli, S. Gossler, S. Lichtenberg, G. Kass, A.K. Agrawal, M. Valerius, K. P. Kinzel, O. Deutschmann, *Angew. Chem. Int. Ed.* 60 (2021) 11852–11857.
[53] A. Çelik, A.B. Shirsath, F. Syla, H. Müller, P. Lott, O. Deutschmann, J. Anal. Appl. Pyrolysis 181 (2024) 106628.
[54] C. Guéret, M. Daroux, F. Billaud, *Chem. Eng. Sci.* 52 (1997) 815–827.
[55] O. Deutschmann, S. Tischer, S. Kleditzsch, V. Janardhanan, C. Correa, D. Chatterjee, N. Mladenov, H. D. Minh, H. Karadeniz, M. Hettel, V. Menon, A. Banerjee, H. Gossler, A. B. Shirsath, E. Daymo, DETCHEM Software package, 2.9 ed., www.detchem.com, Karlsruhe 2022.
[56] S. Wan, K. Keller, P. Lott, A.B. Shirsath, S. Tischer, T. Häber, R. Suntz, O. Deutschmann, *Catal. Sci. Technol.* 12 (2022) 4456–4470.
[57] A.B. Shirsath, M. Mokashi, R. Pashminehazar, A. Çelik, P. Lott, S. Tischer, J.-D. Grunwaldt, O. Deutschmann, *Carbon* 231 (2025) 119689.
[58] G. Blanquart, P. Pepiot-Desjardins, H. Pitsch, *Combust. Flame* 156 (2009) 588–607.
[59] M. Frenklach, *Symp. (int.) Combust.* 26 (1996) 2285–2293.
[60] S. Arora, R. Prasad, *RSC Adv.* 6 (2016) 108668–108688.
[61] J. Pasel, R.C. Samsun, D. Schmitt, R. Peters, D. Stolten, *J. Power Sources* 152 (2005) 189–195.
[62] J. Hunt, A. Ferrari, A. Lita, M. Crosswhite, B. Ashley, A.E. Stiegman, *J. Phys. Chem. C* 117 (2013) 26871–26880.
[63] M. Mokashi, A.B. Shirsath, S. Demir, A. Çelik, P. Lott, S. Tischer, O. Deutschmann, *React Chem. Eng.* 9 (2024) 2902–2914.
[64] L.C.S. Kahle, T. Roussière, L. Maier, K. Herrera Delgado, G. Wasserschaff, S. A. Schunk, O. Deutschmann, *Ind. Eng. Chem. Res.* 52 (2013) 11920–11930.
[65] M. Baigmohammadi, V. Patel, S. Nagaraja, A. Ramalingam, S. Martinez, S. Panigrahy, A.A.E.-S. Mohamed, K.P. Somers, U. Burke, K.A. Heufer, A. Pekalski, H.J. Curran, Energy Fuels 34 (2020) 8808–8823.
[66] A. Punia, L. Kostiuk, J. Olfert, M. Secanell, *Chem. Eng. J.* 502 (2024) 157994.
[67] C. Wei, M. Abuseada, B. Jeevaretanam, T.S. Fisher, R.M. Spearrin, *Proc. Combust. Inst.* 39 (2023) 5581–5589.